https://doi.org/10.1038/s41586-019-1393-y

Signatures of tunable superconductivity in a trilayer graphene moiré superlattice

Guorui Chen[1,2,13], Aaron L. Sharpe[3,4,13], Patrick Gallagher[1,2], Ilan T. Rosen[3,4], Eli J. Fox[4,5], Lili Jiang[2], Bosai Lyu[6,7], Hongyuan Li[6,7], Kenji Watanabe[8], Takashi Taniguchi[8], Jeil Jung[9], Zhiwen Shi[6,7], David Goldhaber-Gordon[4,5]*, Yuanbo Zhang[7,10,11]* & Feng Wang[1,2,12]*

Understanding the mechanism of high-transition-temperature (high-T_c) superconductivity is a central problem in condensed matter physics. It is often speculated that high-T_c superconductivity arises in a doped Mott insulator[1] as described by the Hubbard model[2–4]. An exact solution of the Hubbard model, however, is extremely challenging owing to the strong electron–electron correlation in Mott insulators. Therefore, it is highly desirable to study a tunable Hubbard system, in which systematic investigations of the unconventional superconductivity and its evolution with the Hubbard parameters can deepen our understanding of the Hubbard model. Here we report signatures of tunable superconductivity in an ABC-trilayer graphene (TLG) and hexagonal boron nitride (hBN) moiré superlattice. Unlike in 'magic angle' twisted bilayer graphene, theoretical calculations show that under a vertical displacement field, the ABC-TLG/hBN heterostructure features an isolated flat valence miniband associated with a Hubbard model on a triangular superlattice[5,6] where the bandwidth can be tuned continuously with the vertical displacement field. Upon applying such a displacement field we find experimentally that the ABC-TLG/hBN superlattice displays Mott insulating states below 20 kelvin at one-quarter and one-half fillings of the states, corresponding to one and two holes per unit cell, respectively. Upon further cooling, signatures of superconductivity ('domes') emerge below 1 kelvin for the electron- and hole-doped sides of the one-quarter-filling Mott state. The electronic behaviour in the ABC-TLG/hBN superlattice is expected to depend sensitively on the interplay between the electron–electron interaction and the miniband bandwidth. By varying the vertical displacement field, we demonstrate transitions from the candidate superconductor to Mott insulator and metallic phases. Our study shows that ABC-TLG/hBN heterostructures offer attractive model systems in which to explore rich correlated behaviour emerging in the tunable triangular Hubbard model.

The ability to exfoliate and stack atomically thin two-dimensional materials into new classes of van der Waals heterostructures has ushered in a new era for synthetic quantum materials. The properties of such heterostructures can be conveniently controlled through both the composition and stacking orientation of different layered materials and an external electrical field from electrostatic gates. The power of this approach has recently been demonstrated by reports of correlated insulating states and superconductivity in magic-angle twisted bilayer graphene[7,8] and gate-tunable Mott insulating states in ABC-TLG/hBN heterostructures[5]. In particular, the ABC-TLG/hBN system provides an ideal platform for systematic study of the triangular Hubbard model with fourfold onsite degeneracy: theoretical calculations show that the system features an isolated nearly flat miniband in a triangular superlattice and the miniband's bandwidth can be tuned with a vertical electric field. By contrast, calculations for magic-angle twisted bilayer graphene show two nearly flat minibands that always intersect in the single-particle bandstructure[8]. Here we report signatures of tunable superconductivity in an ABC-TLG/hBN heterostructure around the 1/4-filling Mott state, corresponding to one hole per unit cell in the moiré superlattice. Two apparent superconducting domes are observed with electron and hole doping relative to the 1/4-filling Mott state. In addition, transitions between superconducting, insulating and metallic states in the ABC-TLG/hBN heterostructure are readily controlled by a vertical electric field.

The sample fabrication process is similar to that reported in ref. [8]. In brief, near-field infrared nanoscopy is used to identify ABC and ABA regions in exfoliated TLG[9]. Dry transfer methods are used to pick up and assemble hBN/ABC-TLG/hBN stacks with careful angular alignment[10,11]. Standard electron-beam lithography, reactive ion etching and electron-beam evaporation are used to fabricate ABC-TLG/hBN devices in a Hall bar geometry. The TLG is contacted through one-dimensional edge contacts with non-superconducting Cr/Au metals. We further deposit a metal top electrode to form dual-gated devices in which the TLG/hBN heterostructures can be gated by both the top metal electrode and the bottom silicon substrate. Figure 1a shows an optical image of a fabricated device. The dual-gate configuration allows us to control the carrier concentration and miniband bandwidth of the ABC-TLG/hBN heterostructure independently[12–14]: the bandwidth is tuned by the vertical displacement field $D=\frac{1}{2}(D_b+D_t)$ and the charge concentration relative to the charge neutrality point is $n=(D_b-D_t)/e$, where $D_b=+\varepsilon_b(V_b-V_b^0)/d_b$ and $D_t=-\varepsilon_t(V_t-V_t^0)/d_t$ can be controlled by the bottom and top gate voltages, respectively. Here ε_b and ε_t are the dielectric constants of the bottom (top) dielectric layers and d_b and d_t are the thicknesses of the bottom (top) dielectric layers, and V_b^0 and V_t^0 are the effective offsets in the bottom and top gate voltages caused by environment-induced carrier doping. e is the charge on the electron.

ABC-stacked TLG features a cubic energy dispersion and therefore a large effective mass at low energy[15–18]. In an ABC-TLG/hBN heterostructure in which the TLG is rotationally aligned to one of the hBN cladding layers, a moiré superlattice with a period of 15 nm folds the pristine TLG electronic band into a series of moiré minibands in the first moiré mini Brillouin zone[5,19–23]. Theoretical calculations show that the moiré superlattice in such an ABC-TLG/hBN heterostructure generates a periodic potential characterized by a triangular lattice, yielding first electron and hole minibands with very narrow energy bandwidth (see Methods and Extended Data Figs. 1 and 2 for details of the calculation). A schematic of the triangular ABC-TLG/hBN moiré

---

[1] Materials Science Division, Lawrence Berkeley National Laboratory, Berkeley, CA, USA. [2] Department of Physics, University of California at Berkeley, Berkeley, CA, USA. [3] Department of Applied Physics, Stanford University, Stanford, CA, USA. [4] Stanford Institute for Materials and Energy Sciences, SLAC National Accelerator Laboratory, Menlo Park, CA, USA. [5] Department of Physics, Stanford University, Stanford, CA, USA. [6] Key Laboratory of Artificial Structures and Quantum Control (Ministry of Education), School of Physics and Astronomy, Shanghai Jiao Tong University, Shanghai, China. [7] Collaborative Innovation Center of Advanced Microstructures, Nanjing, China. [8] National Institute for Materials Science, Tsukuba, Japan. [9] Department of Physics, University of Seoul, Seoul, South Korea. [10] State Key Laboratory of Surface Physics and Department of Physics, Fudan University, Shanghai, China. [11] Institute for Nanoelectronic Devices and Quantum Computing, Fudan University, Shanghai, China. [12] Kavli Energy NanoSciences Institute at the University of California, Berkeley, CA, USA. [13] These authors contributed equally: Guorui Chen, Aaron L. Sharpe. *e-mail: goldhaber-gordon@stanford.edu; zhyb@fudan.edu.cn; fengwang76@berkeley.edu

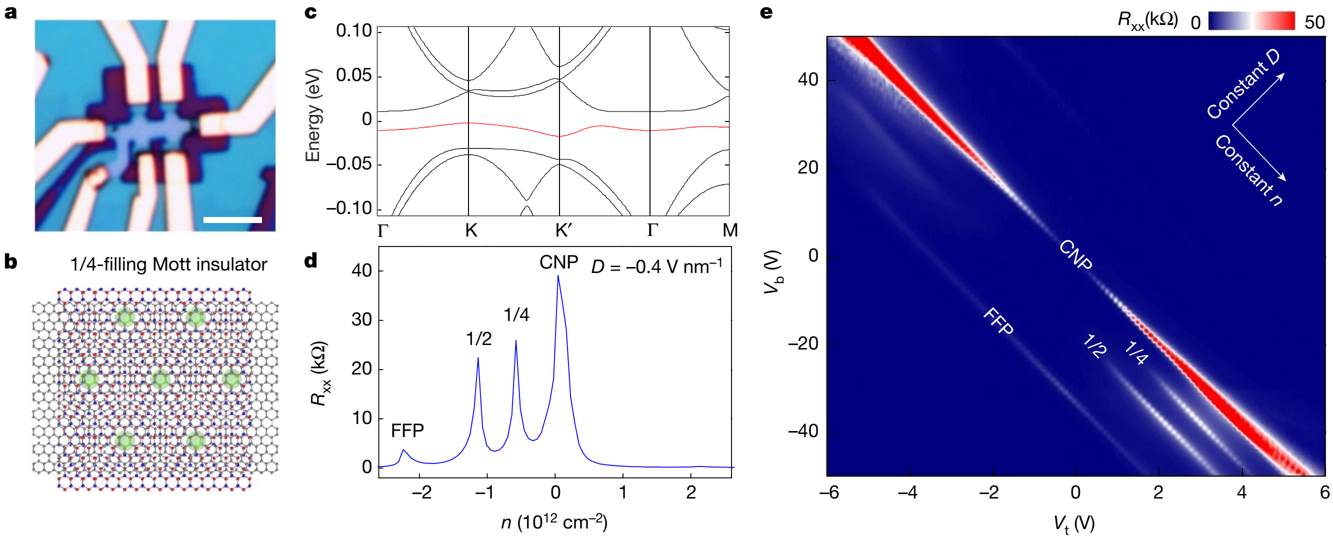

Fig. 1 | Mott insulator in trilayer graphene/hBN moiré superlattice. **a**, An optical image of the ABC-TLG/hBN device with top and bottom gates. Scale bar, 3 μm. **b**, A schematic of the triangular ABC-TLG/hBN moiré superlattice and the 1/4-filling Mott insulating state, which corresponds to one hole per superlattice unit cell. **c**, The single-particle energy dispersion of the lowest electron and hole minibands in the ABC-TLG/hBN superlattice with an effective potential energy difference between the bottom and top graphene layer of $2\Delta = -20$ meV, which can be generated by a vertical displacement field of -0.4 V nm^{-1}. It features a narrow and isolated hole miniband, shown highlighted in red. **d**, R_{xx} as a function of carrier density shows prominent Mott insulating states at 1/4 and 1/2 fillings with $D = -0.4$ V nm^{-1} at $T = 5$ K. **e**, Two-dimensional colour plot of R_{xx} as a function of V_t and V_b at $T = 5$ K. The resistance peaks at 1/4 and 1/2 fillings of the first hole miniband can be clearly identified for relatively large D.

superlattice is shown in Fig. 1b, c displays the calculated energy dispersion of the lowest electron and hole minibands at the K point for an ABC-TLG/hBN heterostructure in which the moiré superlattice is formed with the top hBN flake and the potential energy difference between the bottom and top graphene layers is $2\Delta = -20$ meV (corresponding to the vertical displacement field $D = -0.4$ V nm^{-1} (ref. [5]), where the negative sign denotes that the field is pointing downward). In the ABC-TLG/hBN moiré superlattice, each miniband comprises a time-reversed pair of dispersions centred around the K and K′ valleys in the original graphene Brillouin zone, where $E_K(p) = E_{K'}(-p)$, for a combined fourfold spin and valley degeneracy.

According to our theoretical calculations, strong asymmetry between an electron and a hole exists in the ABC-TLG/hBN system. The first hole miniband is narrower and better separated from the other bands than the first electron miniband. At $2\Delta = -20$ meV, the first hole miniband has a bandwidth W of 11.7 meV and is separated from other bands by over 10 meV. The on-site Coulomb repulsion energy, on the other hand, can be estimated by $U \approx \frac{e^2}{4\pi\varepsilon_0\varepsilon L_M}$. For the moiré lattice constant $L_M = 15$ nm and an hBN dielectric constant $\varepsilon = 4$, U is around 25 meV, which is larger than the value of W. This dominant on-site Coulomb repulsion can lead to Mott insulator states in the flat and isolated hole miniband[5,24,25]. Experimentally, the gate-dependent four-probe resistance (R_{xx}) at a vertical displacement field of -0.4 V nm^{-1} in an ABC-TLG/hBN superlattice is shown in Fig. 1d for a temperature of 5 K. Prominent Mott insulating states are observed at 1/4 and 1/2 fillings of the hole miniband, corresponding to one hole and two holes per superlattice unit cell, respectively. The two-dimensional colour plot of R_{xx} as a function of V_t and V_b in Fig. 1e shows the evolution of the charge neutral point (CNP), 1/4 filling, 1/2 filling, and full filling point (FFP) resistance peaks with the displacement field D. For relatively large D, resistance peaks can be clearly identified at 1/4 and 1/2 fillings of the first hole miniband. As suggested above, the different behaviours of the positive and negative displacement fields arises from the fact that the moiré superlattice exists only at the top hBN/TLG interface in this device.

Signatures of superconductivity emerge in this device below 1 K. We first focus on a state close to the well-developed 1/4-filling Mott insulator with $D = -0.54$ V nm^{-1} and $n = -5.4 \times 10^{11}$ cm^{-2}. (The carrier density at full filling is $n = -2.24 \times 10^{12}$ cm^{-2}). The first sign of superconductivity is a sharp drop of R_{xx} from about 5 kΩ to about 300 Ω within the narrow temperature range of 2 K to 0.2 K. The resistance then remains nearly constant from 0.2 K down to 0.04 K. An empirical fit to the Aslamazov–Larkin formula[26] of the R_{xx}–T curve, shown as the solid line in Fig. 2a, yields an estimated superconducting T_c of 0.65 K. Non-zero residual resistance can appear in measurements of microscopic superconducting samples with poor electrical contacts, as reported in some magic-angle twisted bilayer graphene samples[27] and other two-dimensional superconductors[28,29]. The residual resistance may also have a contribution from non-equilibrium quasiparticles in microscopic devices[30].

A second signature of superconductivity comes from measurements of the current–voltage relationship (I–V curves), as displayed in Fig. 2b. At the lowest temperatures, the I–V curves show a plateau below a critical current of about 10 nA. The plateau region tilts and exhibits nearly linear behaviour at higher temperature. Figure 2c shows the differential resistance dV/dI as a function of driving current, which provides a better visualization of the critical current of about 10 nA below 0.3 K and the evolution to a normal metal behaviour above about 1 K.

Figure 2d displays the critical current behaviour in dV/dI–I curves as a function of the perpendicular magnetic field $B_\perp$ at a base temperature of 40 mK. There is a clear suppression of the apparent superconductivity by the magnetic field, where the superconductivity almost disappears at $B_\perp \approx 0.7$ T. Between 0.7 T and 2 T, the differential resistance at low bias is relatively small and it exhibits a weak nonlinear I–V behaviour (Fig. 2e). However, further measurement of the R–T response at such magnetic fields shows a behaviour characteristic of a metallic state with a weak temperature dependence (see Extended Data Fig. 3).

Figure 2f further displays the in-plane magnetic field dependence of the critical supercurrent behaviour at 40 mK. Figure 2f displays the dV/dI–I curves as a function of the in-plane magnetic field, $B_\parallel$, at 40 mK. The apparent superconductivity in the device is suppressed by $B_\parallel$, with the plateau vanishing above 0.7 T. At the same time, we observe an anomalous resistance peak close to zero current bias at large in-plane magnetic field. We do not know its origin and further experimental and theoretical studies will be needed to fully understand this in-plane magnetic field dependence.

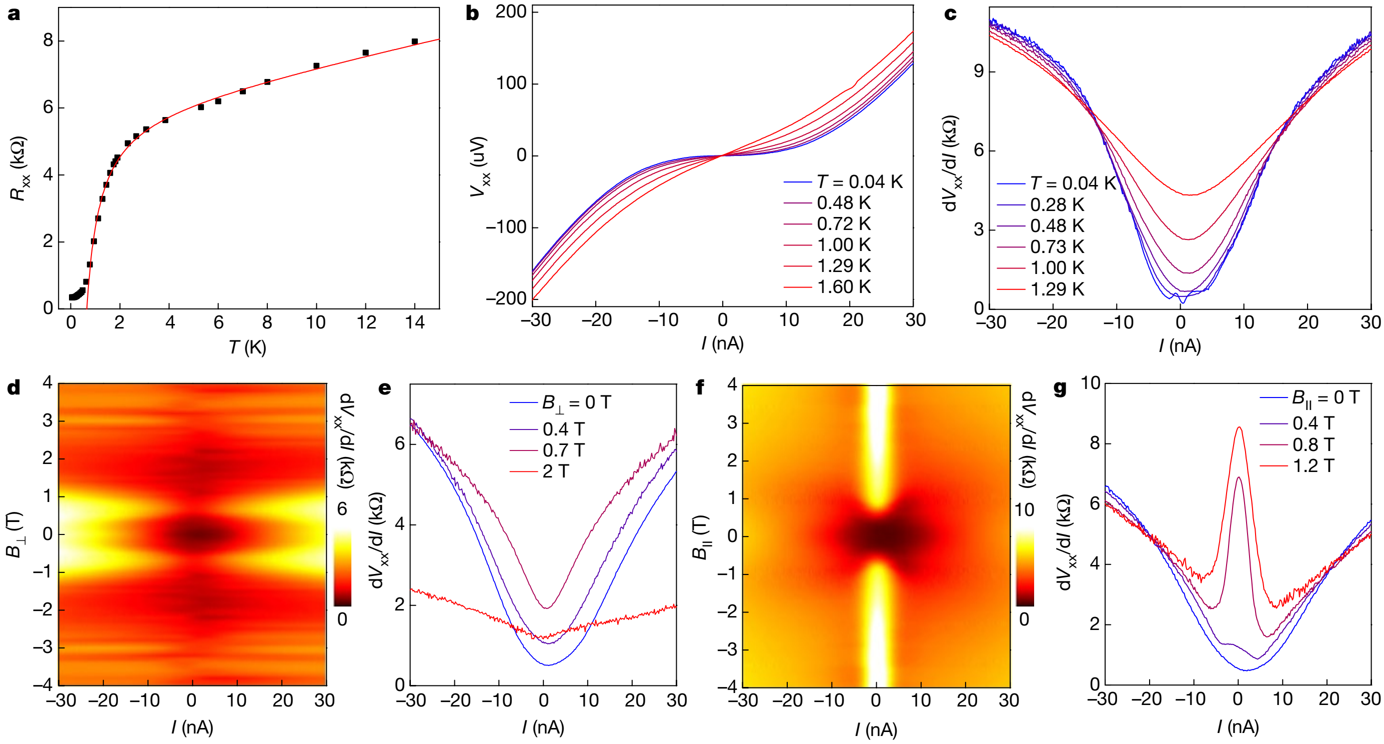

Fig. 2 | Superconductivity in ABC-TLG/hBN. **a**, The R_{xx}–T curve at $D = -0.54$ V nm^{-1} and $n = -5.4 \times 10^{11}$ cm^{-2} shows characteristic behaviour of a superconducting transition. An empirical fit to the Aslamazov–Larkin formula (red line) yields an estimated superconducting temperature of 0.65 K. **b**, I–V curves at different temperatures show a plateau below the critical current at about 10 nA for temperatures below 0.3 K. This plateau region tilts and becomes close to linear at higher temperature, characteristic of a superconducting transition. **c**, dV_{xx}/dI–I curves at different temperatures. A critical current of about 10 nA is observed at the lowest temperatures. **d**, The dV_{xx}/dI colour plot as a function of direct current (d.c.) bias current and perpendicular magnetic field at $T = 0.04$ K. **e**, Line cuts of **d** at $B_{\perp} = 0$ T, 0.4 T, 0.7 T and 2 T. **f**, The dV/dI colour plot as a function of d.c. bias current and in-plane magnetic field at $T = 0.04$ K. **g**, Line cuts of **f** at $B_{//} = 0$ T, 0.4 T, 0.8 T and 1.2 T. A symmetrized $V_{xx}(B) = [V_{xx}(+B) + V_{xx}(-B)]/2$ is presented to remove any possible V_{xy} component in panels **d**–**g**.

Next, we examine the superconductivity phase diagram as a function of T and n. We fix D at two different values: $D = -0.54$ V nm^{-1}, where both the 1/2- and 1/4-filling Mott states appear (Fig. 3a); and $D = -0.17$ V nm^{-1}, where only the 1/2-filling Mott state appears (Fig. 3b).

At $D = -0.54$ V nm^{-1}, two apparent superconducting domes emerge at low temperature near the 1/4-filling Mott state: superconductivity appears to exist for both electron and hole doping relative to the 1/4-filling Mott state, analogous to the behaviour seen in high-T_c copper oxides[3]. This also resembles the behaviour observed in magic-angle twisted bilayer graphene around 1/2 hole filling[8], although more recent work suggests that lower disorder produces only one dome, at slight hole doping relative to the Mott insulator[27]. The presence of superconductivity even at 1/4-filling in our measurements may be attributed to

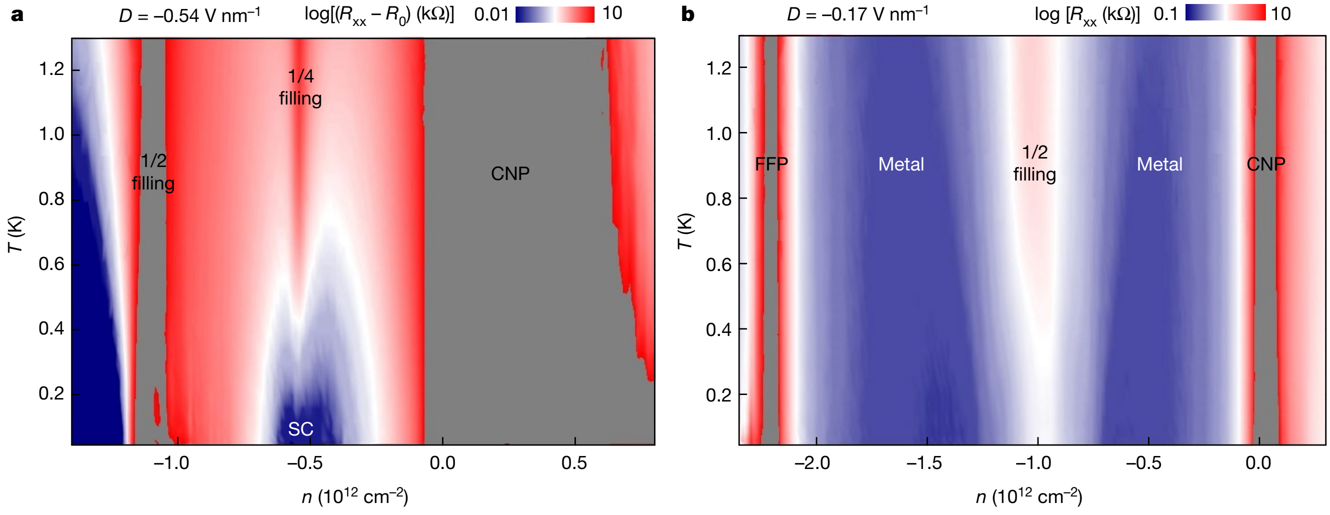

Fig. 3 | Carrier-density-dependent phase diagram. R_{xx} as a function of carrier density and temperature at $D = -0.54$ V nm^{-1} (**a**) and $D = -0.17$ V nm^{-1} (**b**). The superconducting (SC) phase emerges at low temperature near the 1/4-filling Mott state for $D = -0.54$ V nm^{-1}. Only the 1/2-filling Mott state exists for $D = -0.17$ V nm^{-1}, and no superconductivity state exists even at base temperature. Both the superconducting phase and the metal phase show very small resistance values at base temperature, but they can be distinguished by the supercurrent behaviour in the I–V and dV/dI curves and by the R–T dependence (Fig. 4b versus Fig. 4d). Colour scale, $R_0 = 380$ Ω.

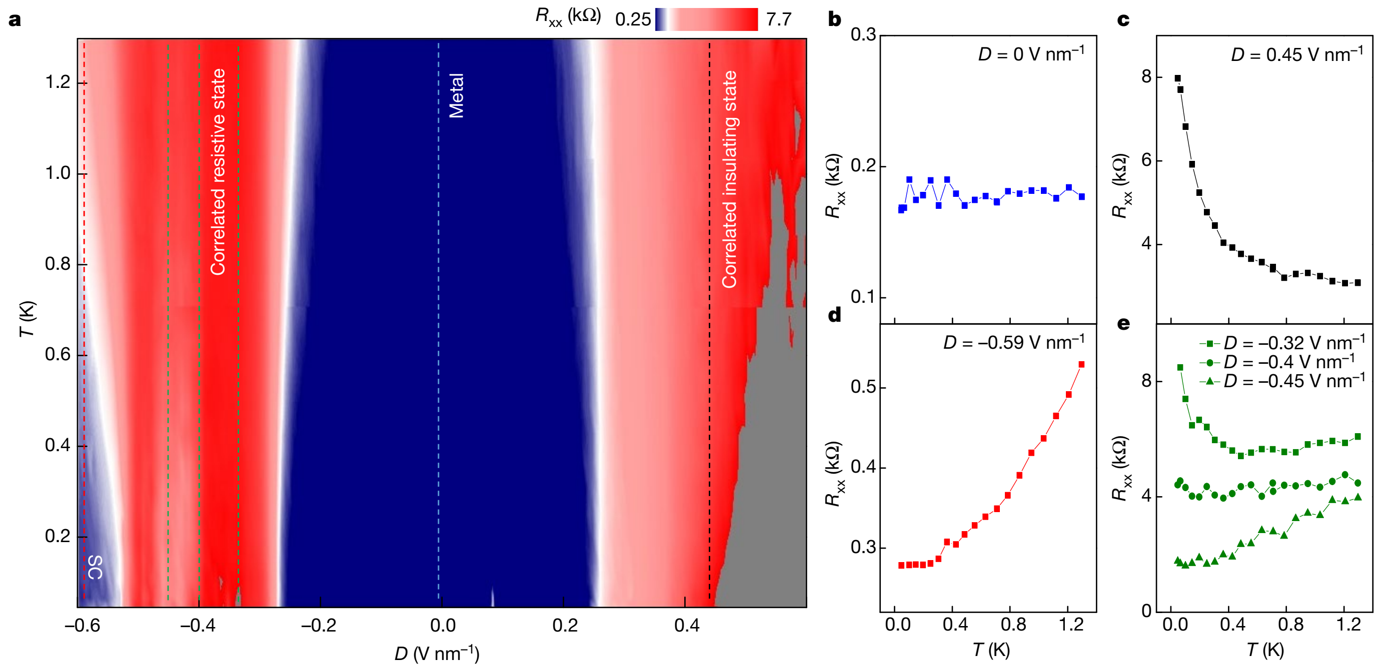

Fig. 4 | Tunable electronic phases with the displacement field. a, R_{xx} as a function of D and T at fixed doping $n = -5.2 \times 10^{12}$ cm^{-2} relative to CNP, corresponding to slight electron doping relative to 1/4-hole filling. D modifies the band structure of the minibands in ABC-TLG/hBN, and therefore the charge correlations. As a function of D, the system can be tuned across four different electronic states from left to right: superconducting, correlated resistive state, metal and correlated insulating state. **b**–**e**, Vertical line cuts of **a** at selected D values to illustrate the R_{xx}–T behaviour of different electronic states. **b**, The metallic state at $D = 0$ V nm^{-1} shows a low and constant resistance owing to the dominating impurity scattering. **c**, The correlated insulating state at $D = 0.45$ V nm^{-1} shows an increased resistance at lower temperature. **d**, The superconducting state at $D = -0.59$ V nm^{-1} shows a rapidly decreasing resistance to a constant residual value at low temperature. **e**, The transition region between $D = -0.28$ V nm^{-1} and -0.53 V nm^{-1} exhibits rather complex behaviour, and we refer to it as a 'correlated resistive state' because the overall resistance is relatively high compared with the metallic region. The state at $D = -0.32$ V nm^{-1} shows a weak insulator-like behaviour with increased resistance at the lowest temperatures, the state at $D = -0.4$ V nm^{-1} shows an almost constant but relatively large resistance value, and the state at $D = -0.45$ V nm^{-1} displays a strange-metal-like behaviour with an almost linear decrease of resistance at low temperature.

the charge inhomogeneity in the trilayer graphene devices (see detailed discussions in the Methods), which can lead to patches of superconductivity when the average filling corresponds to a Mott insulator, as seen at higher temperatures (see Extended Data Fig. 4). The behaviour around the 1/2-filling Mott state is less clear, perhaps reflecting a weaker superconducting state. The resistance remains rather high on the electron-doping side of the 1/2-filling point. The R–T curve for hole doping relative to the 1/2-filling Mott state is consistent with a superconducting transition, but the I–V curve shows a very weak plateau (see Methods and Extended Data Fig. 5). Further studies will be required to establish the nature of this state.

At $D = -0.17$ V nm^{-1}, where only the 1/2-filling Mott state exists, the phase diagram shows no superconductivity even at base temperature. The metal phases show very small resistance values at base temperature, but they can be distinguished from superconducting phases by their R–T dependences and the lack of nonlinear behaviour in the I–V and dV/dI curves.

The ABC-TLG/hBN system offers a platform with which to investigate the evolution of superconductivity where the bandstructure of the miniband can be continuously tuned by D. We fix the carrier concentration at a constant $n = -5.2 \times 10^{11}$ cm^{-2}, which corresponds to a small electron doping relative to the 1/4-filling Mott states, and examine the electronic phases at different D. The four-probe resistance R_{xx} as a function of D and T is displayed as a two-dimensional colour plot in Fig. 4a. At small D where the miniband bandwidth is relatively broad, the system exhibits a metallic phase. Figure 4b shows the R_{xx}–T plot at $D = 0$, where the resistance is low and constant, suggesting that impurity scattering dominates at very low temperature. When D is increased to a positive value, we observe a phase transition from the metallic state to a correlated insulating state caused by the field-induced narrowing of the hole miniband[5]. A line cut at $D = 0.45$ V nm^{-1} of Fig. 4a shows the insulating R_{xx}–T behaviour of such a correlated insulating state (Fig. 4c). Superconductivity, however, never appears for positive D at this n. As D is decreased, we observe an evolution from the metallic phase ($D > -0.28$ V nm^{-1}) to a candidate superconducting phase ($D < -0.53$ V nm^{-1}) (we limited $|D|$ to 0.6 V nm^{-1} to avoid possible damage to the gate dielectrics). The transition region between $D = -0.28$ V nm^{-1} and -0.53 V nm^{-1} exhibits complex behaviour, and we refer to it as a 'correlated resistive state' because the overall resistance is relatively high compared with the metallic region. Figure 4e shows several R–T curves with different behaviours in this transition region.

The ABC-TLG/hBN superlattice thus provides a unique model system with which to study the triangular Hubbard model with fourfold onsite degeneracy, associated with an isolated and electrically controllable nearly flat fourfold-degenerate miniband. In this system, we experimentally find tunable Mott insulator states and signatures of tunable superconductivity. Further studies of such a tunable quantum system may shed light on the longstanding question of high-T_c superconductivity's relationship to the Hubbard model. ABC-TLG/hBN systems may also reveal new types of electronic states—such as spin liquid phases[25], electrically tunable Chern bands[6,31], and topological triplet superconductivity[24,32]—all of which have been recently predicted for a triangular Hubbard model based on ABC-TLG/hBN superlattices.

Online content

Any methods, additional references, Nature Research reporting summaries, source data, statements of code and data availability and associated accession codes are available at https://doi.org/10.1038/s41586-019-1393-y.

Received: 1 October 2018; Accepted: 9 May 2019;
Published online 17 July 2019.

1. Mott, N. F. The basis of the electron theory of metals, with special reference to the transition metals. *Proc. Phys. Soc. A* **62**, 416 (1949).
2. Hubbard, J. Electron correlations in narrow energy bands. II. The degenerate band case. *Proc. R. Soc. Lond. A* **277**, 237–259 (1964).

3. Lee, P. A., Nagaosa, N. & Wen, X.-G. Doping a Mott insulator: physics of high-temperature superconductivity. *Rev. Mod. Phys*. **78**, 17–85 (2006).
4. Imada, M., Fujimori, A. & Tokura, Y. Metal-insulator transitions. *Rev. Mod. Phys*. **70**, 1039 (1998).
5. Chen, G. et al. Evidence of a gate-tunable Mott insulator in a trilayer graphene moiré superlattice. *Nat. Phys*. **15**, 237–241 (2019).
6. Chittari, B. L., Chen, G., Zhang, Y., Wang, F. & Jung, J. Gate-tunable topological flat bands in trilayer graphene boron-nitride moiré superlattices. *Phys. Rev. Lett*. **122**, 016401 (2019).
7. Cao, Y. et al. Correlated insulator behaviour at half-filling in magic-angle graphene superlattices. *Nature* **556**, 80–84 (2018).
8. Cao, Y. et al. Unconventional superconductivity in magic-angle graphene superlattices. *Nature* **556**, 43–50 (2018).
9. Ju, L. et al. Topological valley transport at bilayer graphene domain walls. *Nature* **520**, 650–655 (2015).
10. Wang, L. et al. One-dimensional electrical contact to a two-dimensional material. *Science* **342**, 614–617 (2013).
11. Chen, G. et al. Emergence of tertiary Dirac points in graphene moiré superlattices. *Nano Lett*. **17**, 3576–3581 (2017).
12. Lui, C. H., Li, Z., Mak, K. F., Cappelluti, E. & Heinz, T. F. Observation of an electrically tunable band gap in trilayer graphene. *Nat. Phys*. **7**, 944–947 (2011).
13. Zou, K., Zhang, F., Clapp, C., MacDonald, A. H. & Zhu, J. Transport studies of dual-gated ABC and ABA trilayer graphene: band gap opening and band structure tuning in very large perpendicular electric fields. *Nano Lett*. **13**, 369–373 (2013).
14. Lee, Y. et al. Competition between spontaneous symmetry breaking and single-particle gaps in trilayer graphene. *Nat. Commun*. **5**, 5656 (2014).
15. Zhang, F., Sahu, B., Min, H. & MacDonald, A. H. Band structure of ABC-stacked graphene trilayers. *Phys. Rev. B* **82**, 035409 (2010).
16. Koshino, M. & McCann, E. Trigonal warping and Berry's phase $N\pi$ in ABC-stacked multilayer graphene. *Phys. Rev. B* **80**, 165409 (2009).
17. Bao, W. et al. Stacking-dependent band gap and quantum transport in trilayer graphene. *Nat. Phys*. **7**, 948–952 (2011).
18. Zhang, L., Zhang, Y., Camacho, J., Khodas, M. & Zaliznyak, I. The experimental observation of quantum Hall effect of $l=3$ chiral quasiparticles in trilayer graphene. *Nat. Phys*. **7**, 953–957 (2011).
19. Yankowitz, M. et al. Emergence of superlattice Dirac points in graphene on hexagonal boron nitride. *Nat. Phys*. **8**, 382–386 (2012).
20. Dean, C. R. et al. Hofstadter's butterfly and the fractal quantum Hall effect in moiré superlattices. *Nature* **497**, 598–602 (2013).
21. Ponomarenko, L. A. et al. Cloning of Dirac fermions in graphene superlattices. *Nature* **497**, 594–597 (2013).
22. Hunt, B. et al. Massive Dirac fermions and Hofstadter butterfly in a van der Waals heterostructure. *Science* **340**, 1427–1430 (2013).
23. Yang, W. et al. Epitaxial growth of single-domain graphene on hexagonal boron nitride. *Nat. Mater*. **12**, 792–797 (2013).
24. Zhu, G.-Y., Xiang, T. & Zhang, G.-M. Spin-valley antiferromagnetism and topological superconductivity in the trilayer graphene Moire super-lattice. Preprint at https://arxiv.org/abs/1806.07535 (2018).
25. Zhang, Y.-H. & Senthil, T. Bridging Hubbard model physics and quantum Hall physics in trilayer graphene/h-BN moiré superlattice. Preprint at https://arxiv.org/abs/1809.05110 (2018).
26. Aslamasov, L. G. & Larkin, A. I. The influence of fluctuation pairing of electrons on the conductivity of normal metal. *Phys. Lett. A* **26**, 238–239 (1968).
27. Yankowitz, M. et al. Tuning superconductivity in twisted bilayer graphene. *Science* **363**, 1059–1064 (2019).
28. Xi, X. et al. Ising pairing in superconducting $NbSe_2$ atomic layers. *Nat. Phys*. **12**, 139–143 (2016).
29. Fatemi, V. et al. Electrically tunable low density superconductivity in a monolayer topological insulator. *Science* **362**, 926–929 (2018).
30. Yagi, R. Charge imbalance observed in voltage-biased superconductor–normal tunnel junctions. *Phys. Rev. B* **73**, 134507 (2006).
31. Zhang, Y.-H., Mao, D., Cao, Y., Jarillo-Herrero, P. & Senthil, T. Nearly flat Chern bands in moiré superlattices. *Phys. Rev. B* **99**, 075127 (2019).
32. Xu, C. & Balents, L. Topological superconductivity in twisted multilayer graphene. *Phys. Rev. Lett*. **121**, 087001 (2018).

Publisher's note: Springer Nature remains neutral with regard to jurisdictional claims in published maps and institutional affiliations.

METHODS

Sample fabrication. TLG and hBN are mechanically exfoliated on SiO_2/Si substrate and the layer number of TLG is identified by optical contrast and atomic force microscopy. ABC-TLG is characterized by near-field infrared nanoscopy and isolated in situ by cutting with an atomic force microscope. hBN flakes are selected to be thicker than 30 nm and without step edges. We create the hBN/ABC-TLG/hBN heterostructure by stacking different layers with a dry transfer method[26]. We identify the crystal orientation of TLG and hBN using the crystalline edges of the flakes, and manually align the TLG lattice with the hBN flake during the transfer process. The device is then etched into a Hall bar structure using standard electron-beam lithography. The TLG is contacted through one-dimensional edge contacts with Cr/Au electrodes. We further deposit a metal top electrode to form a dual-gate device where the ABC-TLG/hBN heterostructure can be gated by both the top metal electrode and the bottom silicon substrate.

Transport measurements. The device is measured in a dilution refrigerator which achieves a base electron temperature of $T = 0.04$ K, as determined by Coulomb blockade thermometry. Low temperature electronic filtering, including microwave filters, low-pass resistor-capacitor filters, and thermal meanders, is used to anchor the electron temperature as well as to prevent quasiparticle excitations from high frequency noise. Stanford Research Systems SR830 lock-in amplifiers with NF Corporation LI-75A voltage preamplifiers are used to measure the longitudinal resistance R_{xx} of the device with an alternating current (a.c.) bias current of 0.5 nA to 1 nA at a frequency of 7 Hz. A Yokogawa 7651 d.c. voltage source is used in combination with a 100-MΩ bias resistor to add a d.c. bias current to the device. The voltage in the I–V measurements is measured using an Agilent 34401A. In the $\mathrm{d}V/\mathrm{d}I$–I measurements, a small a.c. bias current (0.5 nA) is generated by the lock-in amplifier output voltage in combination with a 1-GΩ bias resistor. This small a.c. current is added on top of the larger d.c. current bias, and the induced differential voltage is measured using the lock-in technique. In-plane magnetic field measurements are performed using an attocube atto3DR two-axis piezo rotator to control the sample orientation with respect to the field.

Band structure calculations. In our transport results, we found important electron–hole asymmetry and asymmetry in the displacement field direction in ABC-TLG/hBN. To understand the two asymmetries, we calculated the band structure (see ref. [5] for calculation details) and show the results in Extended Data Fig. 1.

The single-particle bandstructure of the heterostructure is described by the Hamiltonian $H = H_{\mathrm{ABC}} + V_{\mathrm{M}}$, where H_{ABC} is the TLG Hamiltonian under a weak vertical electrical field, and V_{M} describes the effective potential acting on TLG from the moiré superlattice. The low-energy electronic structure of ABC-stacked TLG can be captured by an effective two-component Hamiltonian in the K valley that describes hopping between the A atom in the top graphene layer and the C atom in the bottom graphene layer[7,8]

$$H_{\mathrm{ABC}} = \frac{v_0^3}{t_1^2}\begin{pmatrix} 0 & (\pi^{+})^3 \\ \pi^3 & 0 \end{pmatrix} + \left(\frac{2v_0v_3p^2}{t_1} + t_2\right)\begin{pmatrix} 0 & 1 \\ 1 & 0 \end{pmatrix} + \left(\frac{2v_0v_4p^2}{t_1} - \Delta'\right)\begin{pmatrix} 1 & 0 \\ 0 & 1 \end{pmatrix}$$
$$+ \left(\frac{3v_0^2p^2}{t_1^2} - 1\right)\Delta''\begin{pmatrix} 1 & 0 \\ 0 & 1 \end{pmatrix} + \Delta\begin{pmatrix} -1 & 0 \\ 0 & 1 \end{pmatrix}$$

where $\pi = p_x + ip_y$, p is the electron momentum, 2Δ is the electron energy difference between the top and bottom layers due to the vertical electrical field $v_i \equiv \left(\frac{\sqrt{3}}{2}\right)at_i/\hbar$, a is the carbon–carbon lattice constant of around 2.46 Å, $\Delta' \approx 0.0122\,\mathrm{eV}$, $\Delta'' \approx -0.0095\,\mathrm{eV}$, and $t_0,\ t_1,\ t_2, t_{3,}t_4$ are tight-binding parameters in ABC-TLG obtained from local-density approximation ab initio calculations with values of 2.62 eV, 0.358 eV, −0.0083 eV, 0.293 eV and 0.144 eV, respectively. We consider that the encapsulated ABC-TLG forms a near-zero-twisting moiré superlattice with the top hBN film. The ABC-TLG/hBN interaction in the K valley can be approximated by a potential of the form $V_{\mathrm{M}}^{\mathrm{A}}(\boldsymbol{r}) = 2\,C_{\mathrm{A}}\,\mathrm{Re}[\mathrm{e}^{\mathrm{i}\varphi_{\mathrm{A}}}f(\boldsymbol{r})]\begin{pmatrix} 0 & 0 \\ 0 & 1 \end{pmatrix}$ acting at the low-energy A site of the effective ABC trilayer in contact with the top hBN film, where $f(\boldsymbol{r}) = \sum_{j=1}^{6}\mathrm{e}^{\mathrm{i}\boldsymbol{q}_j\boldsymbol{r}}(1+(-1)^j)/2$ and $\boldsymbol{q}_j$ are the six reciprocal lattice vectors of the triangular moiré superlattice with $|\boldsymbol{q}_j| = \boldsymbol{q}_{\mathrm{M}} \equiv \frac{4\pi}{\sqrt{3}L_{\mathrm{M}}}$. The hBN layer periodically modulates the potential in the bottom-layer carbon atom whose magnitude and phase parameters are $C_{\mathrm{A}} = -14.88\,\mathrm{meV}$, $\varphi_{\mathrm{A}} = 50.19^{\mathrm{o}}$. We solve the Hamiltonian numerically by direct diagonalization with a momentum cutoff at $5q_{\mathrm{M}}$.

The calculated electron and hole minibands are asymmetric for both positive and negative displacement field. We found that for interlayer potential difference $2\Delta = -20$ meV ($D = -0.4$ V nm^{-1}), the bandwidth of the electron miniband is 27 meV, while the hole miniband bandwidth is about 15 meV. For $2\Delta = 20$ meV ($D = 0.4$ V nm^{-1}), the bandwidths of the electron and hole minibands are similar, whereas the electron miniband has more overlap with other minibands. In both positive and negative displacement fields, the hole miniband has narrower bandwidth and less overlap with other minibands than the electron miniband. The configuration that gives rise to the narrowest hole minibands experimentally exhibits the strongest Mott insulator behaviour at 1/4 and 1/2 fillings. It is also the configuration that shows superconductivity behaviour at low temperature close to the 1/4 filling.

The asymmetry of positive and negative displacement field can be clearly identified from Extended Data Fig. 1. In the negative displacement field, as shown in Extended Data Fig. 1a, the hole miniband shows narrower bandwidth (11.7 meV) and is totally isolated from other minibands compared to the case in Extended Data Fig. 1b, which corresponds to the positive displacement field (bandwidth is 16.2 meV with overlap to the remote band).

Density-of-states distribution in the first hole miniband. We show in Extended Data Fig. 2 the calculated single-particle density of states in ABC-TLG/hBN moiré superlattice at different displacement fields. Extended Data Fig. 2a–c displays the density of states of the first electron and hole moiré minibands, and Extended Data Fig. 2d–f shows the corresponding integrated density of states for the hole miniband. Our calculation shows that there is a van Hove singularity in the hole miniband, and this singularity lies between the 1/4 and 1/2 fillings for all displacement fields. There is no special singularity in the density of states at 1/4 filling in the ABC-TLG/hBN system.

Possible superconductivity in the hole-doped 1/2-filling Mott state. The R–T behaviour for hole-doped 1/2-filling states shows a superconducting-like transition with a relatively high apparent T_{c} in the phase diagram (Fig. 3). On the other hand, the I–V and $\mathrm{d}V/\mathrm{d}I$–I curves of the hole-doped 1/2-filling states at the base temperature shows only very weak signatures of superconducting behaviour. Extended Data Fig. 5 displays the I–V and $\mathrm{d}V/\mathrm{d}I$–I data for a hole-doped 1/2-filling state with $n = -1.38 \times 10^{12}$ cm^{-2} relative to the CNP point, where only a very narrow plateau is observed in the I–V curve and a narrow dip in the $\mathrm{d}V/\mathrm{d}I$–I curve near zero bias. More systematic studies of the hole-doped 1/2 filling in higher-quality samples will be needed to establish the nature of this state.

Superconductivity in a second device. Similar signatures of superconductivity have been observed in a second ABC-TLG/hBN device. Extended Data Fig. 6 shows the characterization of the Mott states in the second device at $T = 1.5$ K. In contrast to the device in the main text, the Mott states of the second device are prominent in the positive displacement field owing to the moiré pattern between the TLG and the bottom hBN.

Extended Data Fig. 7a shows the superconducting R–T curve at $n = 0.56 \times 10^{12}$ cm^{-2}, $D = 0.55$ V nm^{-1}. The resistivity decreases rapidly by over 30 times below 10 K. A small residue resistivity of about 400 Ω is present at base temperature, possibly due to non-ideal contacts.

Extended Data Fig. 7b shows I–V curves at different temperatures. Strongly nonlinear I–V responses characteristic of superconductivity are observed at the base temperature, where the resistivity is close to zero at low bias current, and increases quickly beyond a critical current. At higher temperatures, the I–V responses become more linear. Extended Data Fig. 7c further demonstrates the suppression of the nonlinear superconductivity I–V responses by a vertical magnetic field.

Extended Data Fig. 7d displays the resistivity as a function of the carrier density and temperature. Signatures of superconductivity are observed only close to the 1/4-filling Mott state, similar to that observed in device 1. The low resistivity at 1/4 filling is probably due to the inhomogeneous doping variation within the device.

Absence of Fraunhofer pattern. Upon careful examining the magnetic field dependence of our transport measurements, we do not see any simple Fraunhofer pattern, unlike in some of the work by other groups[8,27] on superconductivity in twisted bilayer graphene. We can speculate on why this might be. First, there are two kinds of spatial inhomogeneity in moiré superlattice devices: inhomogeneity in the moiré lattice spacing and inhomogeneity in the carrier concentration.

In the case of twisted bilayer graphene, the dominant source of inhomogeneity is believed to be variation in the moiré lattice spacing produced by twist angle disorder[27]. Since the superconductivity is very sensitive to twist angle in twisted bilayer graphene, through both band structure and filling of those bands for a given gate voltage, variation in local twist angle could give rise to weakly connected superconducting regions and hence the recently observed Fraunhofer patterns with relatively well-defined periodicity in magnetic field[8,27]. The effective junction area inferred by ref. [27] was 0.5–1 μm^2, consistent with the scale of spatial variations in twist angles observed by TEM in twisted bilayer graphene with a slightly lower twist angle[33]. In a device with an extremely homogenous twist angle throughout the device, no distinguishable Fraunhofer pattern was observed[34]. Therefore, it seems likely that the Fraunhofer arises from inhomogeneity in the moiré lattice spacing.

In our zero-twist-angle ABC-TLG/hBN devices, the moiré lattice spacing is likely to be much more homogeneous than in twisted bilayer graphene. However, our devices do display inhomogeneity in charge density: the full-width at half-maximum (FWHM) of resistance peaks at CNP and FFP at $D = 0$ are around 1.2×10^{11} cm^{-2} and around 2.0×10^{11} cm^{-2}, respectively, suggesting a charge density inhomogeneity of that same order when disorder is unscreened. This charge density inhomogeneity could lead to superconductive patches even at average 1/4 filling and thus explain the lack of a peak in resistance at 1/4 filling at base temperature. Owing to the presence of the metal top gate about 30 nm away and the Si back gate about 330 nm away, we expect charge density fluctuations on length scales above a few hundred nanometres to be strongly suppressed by screening from both the gates, precluding a junction as large as that inferred by ref. [27] in a twisted bilayer graphene device. However, we might expect fluctuations on the length scale of tens of nanometers given the proximity to the top gate (fluctuations on a larger length scale should fall off quadratically owing to the screening of the gate). A junction corresponding to such a length could have a Fraunhofer-pattern field scale comparable to the apparent critical field of 0.7 T, preventing the pattern from being detectable. In principle, it may be possible to isolate a percolative path with one or a few well-defined junctions, perhaps with a large enough area to yield observable coherent transport, but such a path may only exist at elevated temperatures or in a narrow window of gate voltages, making observation of a clear Fraunhofer pattern extremely challenging in this large parameter space. Although evidence of coherent transport would be strongly indicative of superconductivity, we believe it is reasonable not to expect to observe it clearly in measurements of these heterostructures even with superconductivity present.

This reasoning also raises the question of why charge fluctuations on a smaller length scale than that of twist angle disorder apparently do not greatly influence the superconductivity in twisted bilayer graphene. All the twisted bilayer graphene devices that exhibit superconductivity were fabricated with an additional back gate (either metal or graphite) directly on top of the SiO_2 substrate. By contrast, our ABC-TLG/hBN devices lack such an intermediate gate between the graphene and Si back gate. It is therefore plausible that the SiO_2 is the dominant source of charge disorder in these devices, and that future heterostructures with graphite back gates may exhibit more uniform superconductivity[27,35,36].

Data availability

The data that support the findings of this study are available from the corresponding authors upon reasonable request.

33. Yoo, H. et al. Atomic and electronic reconstruction at the van der Waals interface in twisted bilayer graphene. *Nat. Mater*. **18**, 448–453 (2019).
34. Lu, X. et al. Superconductors, orbital magnets, and correlated states in magic angle bilayer graphene. Preprint at https://arxiv.org/abs/1903.06513 (2019)
35. Zibrov, A. et al. Tunable interacting composite fermion phases in a half-filled bilayer-graphene Landau level. *Nature* **549**, 360–364 (2017).
36. Amet, F. et al. Composite fermions and broken symmetries in graphene. *Nat. Commun*. **6**, 5838 (2015).

Acknowledgements We acknowledge discussions with G. Zhang and T. Xiang. G.C. and F.W. were supported as part of the Center for Novel Pathways to Quantum Coherence in Materials, an Energy Frontier Research Center funded by the US Department of Energy, Office of Science, Basic Energy Sciences. A.L.S. was supported by a National Science Foundation Graduate Research Fellowship and a Ford Foundation Predoctoral Fellowship. The work of I.T.R., E.J.F. and D.G.-G. on this project was supported by the US Department of Energy, Office of Science, Basic Energy Sciences, Materials Sciences and Engineering Division, under contract DE-AC02-76SF00515. For dilution fridge support, low-temperature infrastructure and cryostat support were funded in part by the Gordon and Betty Moore Foundation through grant GBMF3429. Part of the sample fabrication was conducted at the Nano-fabrication Laboratory at Fudan University. Y.Z. acknowledges financial support from the National Key Research Program of China (grants 2016YFA0300703 and 2018YFA0305600), the NSF of China (grants U1732274, 11527805, 11425415 and 11421404) and the Strategic Priority Research Program of the Chinese Academy of Sciences (grant XDB30000000). Z.S. acknowledges support from the National Key Research and Development Program of China (grant 2016YFA0302001) and the NSF of China (grants 11574204 and 11774224). K.W. and T.T. acknowledge support from the Elemental Strategy Initiative, conducted by MEXT, Japan and CREST (JPMJCR15F3), JST. J.J. was supported by the Samsung Science and Technology Foundation under project SSTF-BA1802-06 and by the Korean National Research Foundation grant NRF-2016R1A2B4010105.

Author contributions F.W., Y.Z. and D.G.-G. supervised the project. G.C. fabricated samples and performed basic transport characterizations at temperatures above 5 K. G.C., A.L.S., P.G., I.T.R. and E.J.F. performed ultralow temperature transport measurements. G.C., L.J., B.L., H.L. and Z.S. prepared trilayer graphene and performed near-field infrared and atomic force microscope measurements. K.W. and T.T. grew hBN single crystals. J.J. calculated the band structures. G.C., A.L.S., P.G., I.T.R., D.G.-G., Y.Z. and F.W. analysed the data. G.C. and F.W. wrote the paper, with input from all authors.

Competing interests The authors declare no competing interests.

Additional information
Supplementary information is available for this paper at https://doi.org/10.1038/s41586-019-1393-y.
Correspondence and requests for materials should be addressed to D.G., Y.Z. or F.W.
Reprints and permissions information is available at http://www.nature.com/reprints.

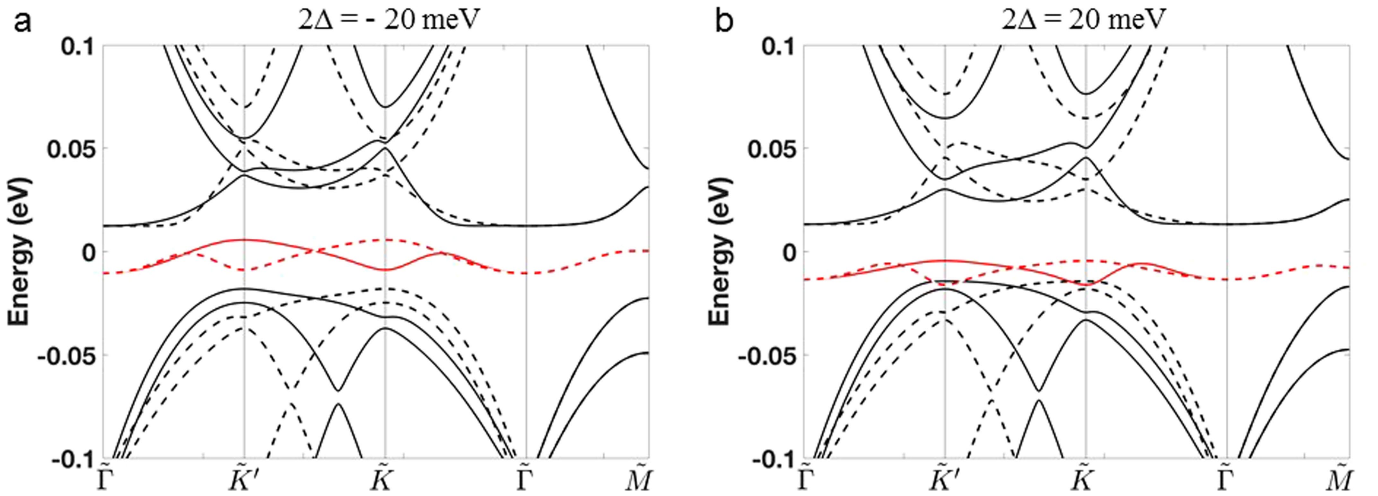

Extended Data Fig. 1 | Calculated band structure of ABC-TLG/hBN. **a**, **b**, Calculated band structure of ABC-TLG/hBN with negative (**a**) and positive (**b**) displacement fields. The solid and dashed lines correspond to band structure at the K and K′ valleys, respectively. The energy difference between top- and bottom-layer graphene $2\Delta = 20$ meV corresponds to the displacement field $D = 0.4$ V nm^{-1}.

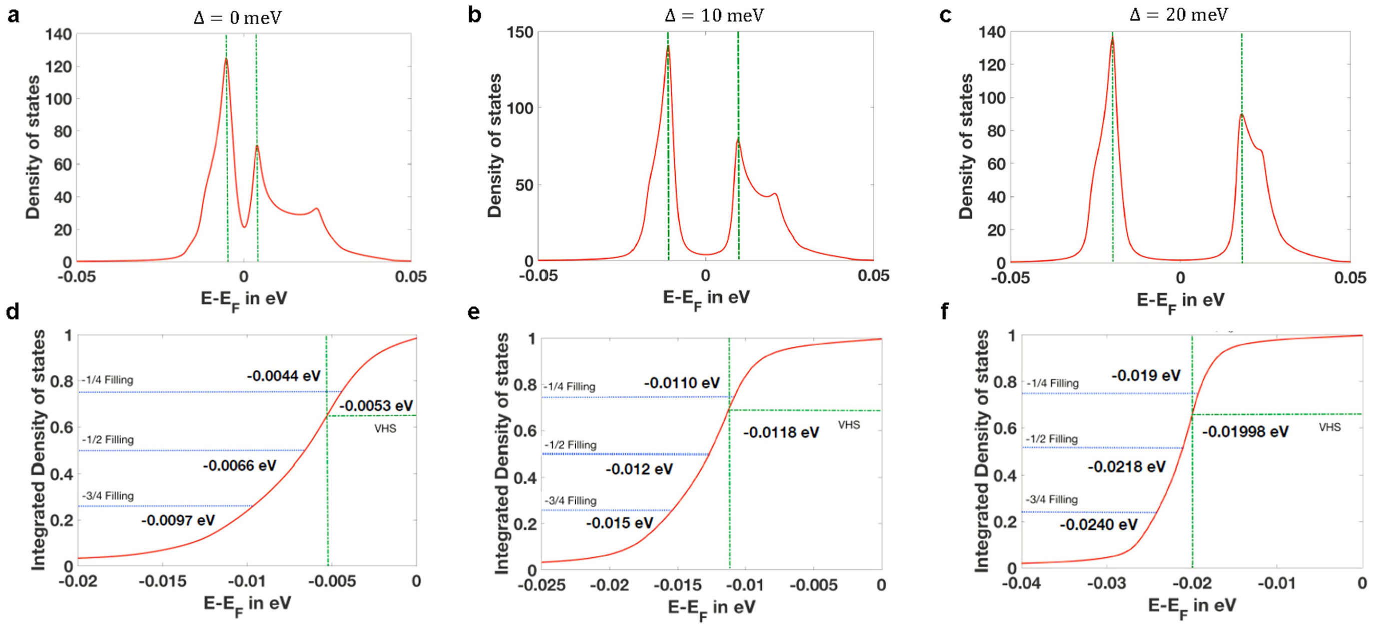

Extended Data Fig. 2 | Calculated density of states. a–**c**, Density of states of the first electron and hole minibands in the single-particle band structure of the ABC-TLG/hBN moiré superlattice with effective potential energy differences between the bottom and top graphene layer of $2\Delta = 0$ meV, 10 meV and 20 meV. **d**–**f**, The integrated density of states corresponding to **a**–**c**, respectively.

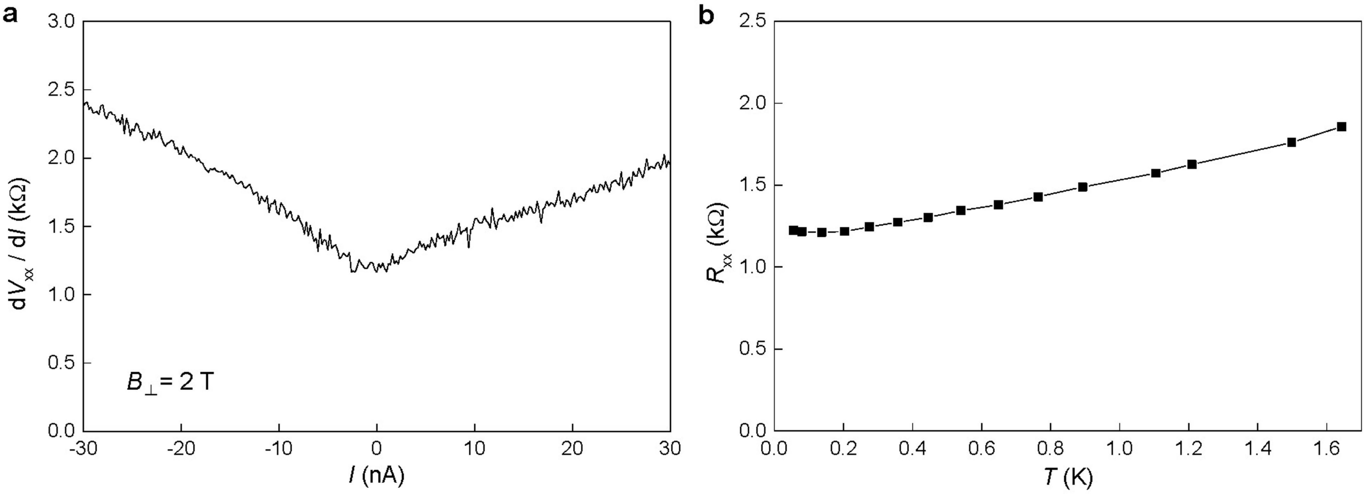

Extended Data Fig. 3 | Transport at $B_{\perp} = 2$ T. **a**, dV_{xx}/dI as a function of d.c. current. **b**, Resistance as a function of temperature at $B_{\perp} = 2$ T.

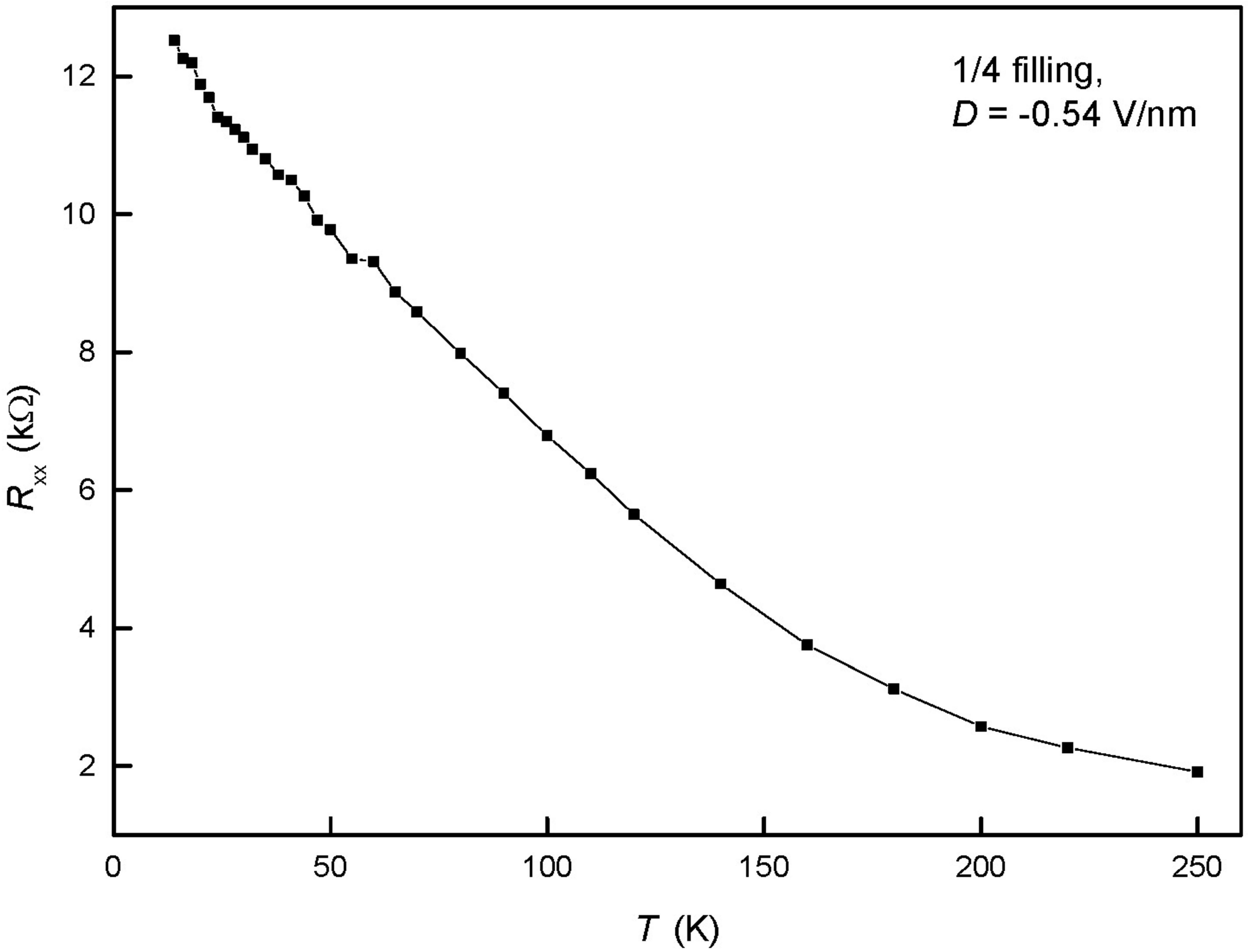

Extended Data Fig. 4 | Temperature-dependent resistance at 1/4 filling at high temperatures. R_{xx} at 1/4 filling as a function of temperatures from 14 K to 250 K, $D = -0.54$ V nm^{-1}, which indicates that the 1/4-filling Mott state has insulating behaviour at high temperatures.

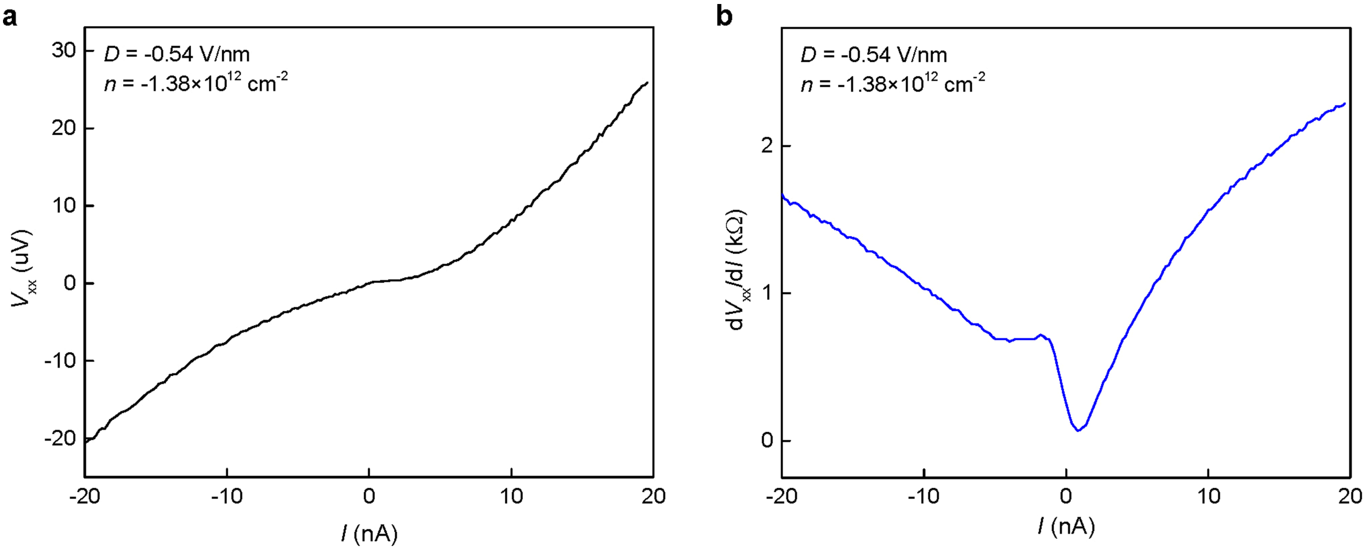

Extended Data Fig. 5 | Possible weak superconductivity at 1/2 filling. V_{xx} and dV_{xx}/dI as a function of the d.c. bias current at a hole-doped 1/2-filling state. The narrow plateau in the I–V curve and the dip of dV_{xx}/dI near zero bias current may be due to very weak superconductivity in this state. Data are taken at $T = 0.04$ K.

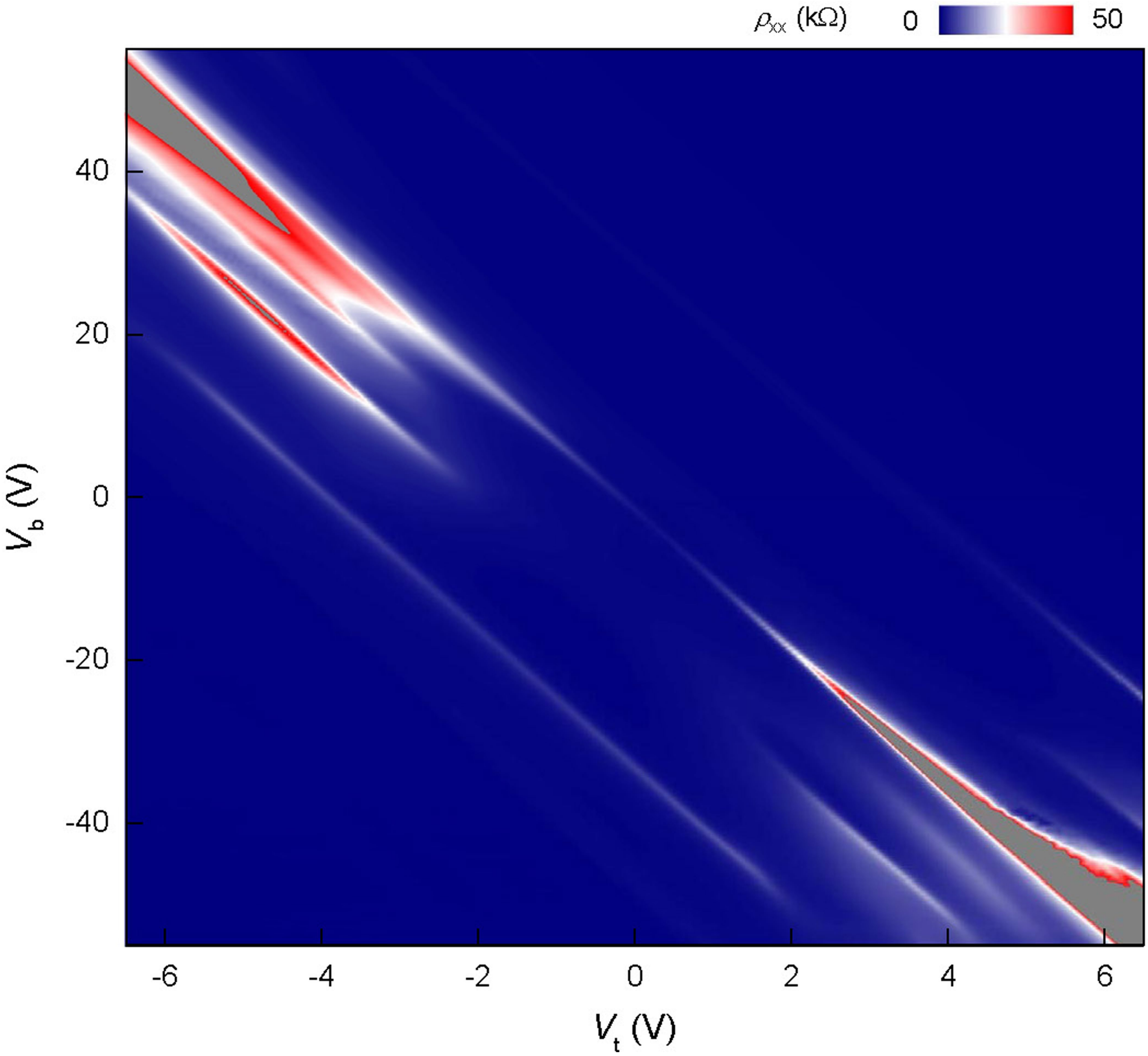

Extended Data Fig. 6 | Transport in a second ABC-TLG/hBN device. Resistivity of the second ABC-TLG/hBN device as a function of V_t and V_b at $T = 1.5$ K.

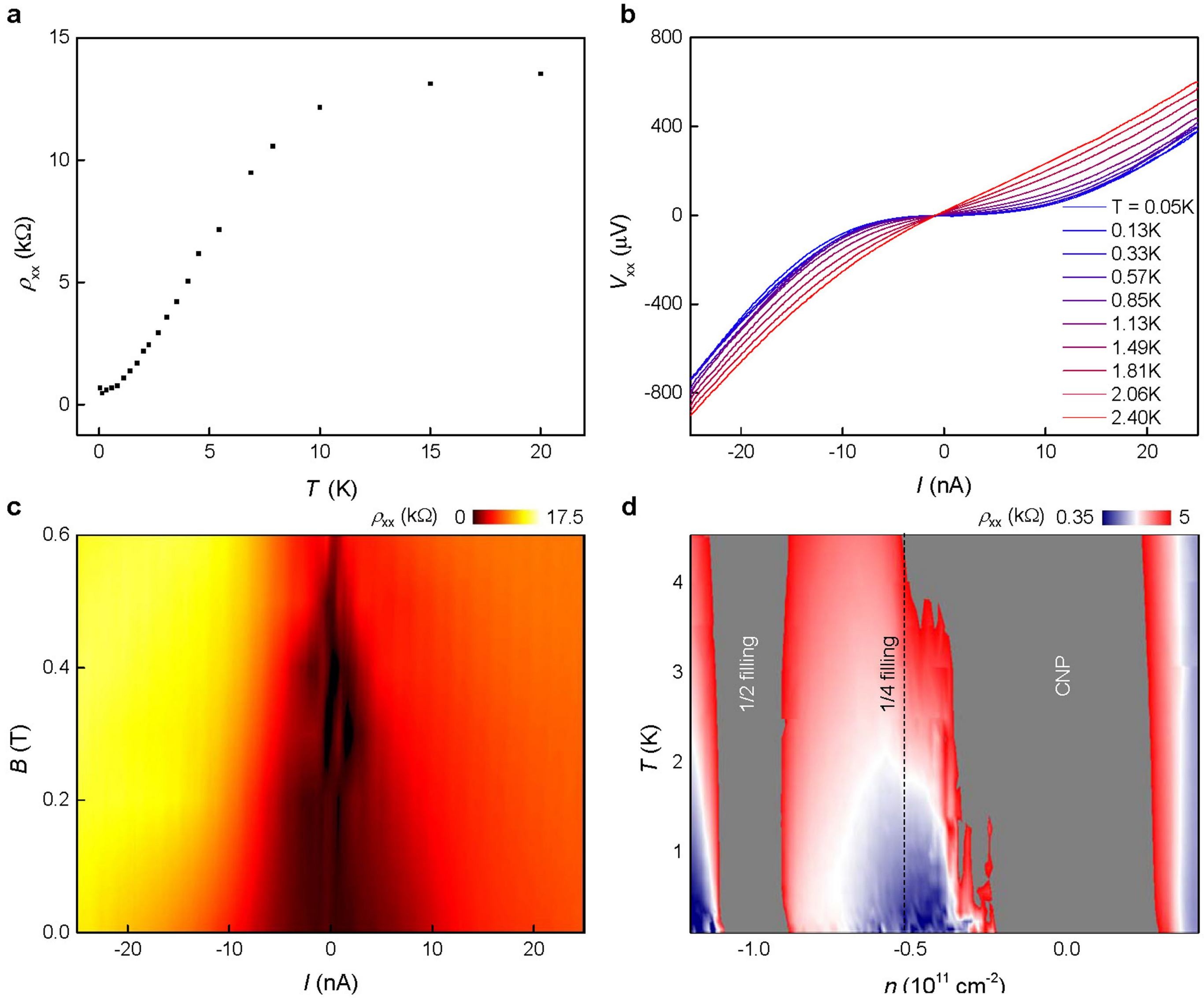

Extended Data Fig. 7 | Signatures of superconductivity in the second ABC-TLG/hBN device. a. Resistivity ρ_{xx}–T curve at $n = 0.56 \times 10^{12}$ cm^{-2}, $D = 0.55$ V nm^{-1}. The high-temperature data above 10 K were measured during a separate cooldown. **b**, I–V curves at different temperatures, showing a plateau below the critical current of about 6 nA below $T = 0.57$ K. This plateau region tilts and becomes close to linear at higher temperature, characteristic of a superconducting transition. **c**, The dV/dI colour plot as a function of d.c. bias current and perpendicular magnetic field at $T = 0.05$ K. The superconductivity is suppressed by the magnetic field and almost disappears at $B \approx 0.6$ T. **d**, Carrier-density-dependent phase diagram at $D = 0.55$ V nm^{-1}. The dashed line corresponds to the 1/4 filling.